Contrasting Transport and Electrostatic Properties of Selectively Fluorinated Alkanethiol Monolayers with Embedded Dipoles

Robert C. Bruce,[†,*] Lin You,[†,‡] Anja Förster,[§] Sujitra Pookpanratana,[†] Olivia Pomerenk,[†] Han Ju Lee,[∥] Maria D. Marquez,[∥] Rashid Ghanbaripour,[∥] Oussama Zenasni,[∥] T. Randall Lee,[∥] and Christina A. Hacker[†,*]

[†]Engineering Physics Division, National Institute of Standards and Technology, Gaithersburg, Maryland 20899-8120, United States
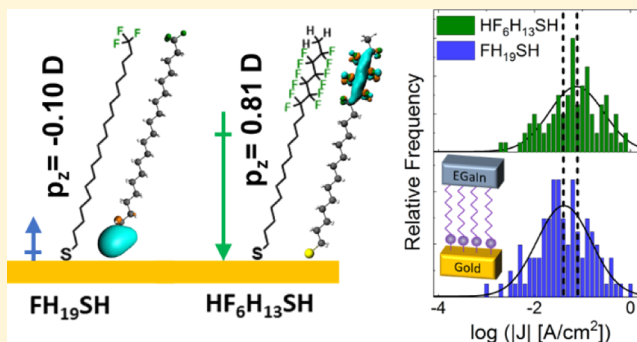
[‡]Theiss Research, La Jolla, California 92037, United States

[§]Department of Theoretical Chemistry, Technische Universität Dresden, 01062 Dresden, Germany

[∥]Department of Chemistry and the Texas Center for Superconductivity, University of Houston, Houston, Texas 77204-5003, United States

S *Supporting Information*

ABSTRACT: Surface dipoles are a powerful tool in interfacial modification for improving device output via energy level matching. Fluorinated alkanethiols show a strong promise for these applications as they can generate large and tunable dipoles based on fluorine location and chain length. Furthermore, these chains can be designed to possess fluorocarbons solely along the backbone, enabling an "embedded" configuration that generates a significant dipole effect from the fluorines while maintaining surface chemistry to prevent deleterious side effects from altered surface interactions. However, fluorine substitution can modify other molecular electronic properties, and it is important to consider the transport properties of these interfacial modifiers so that knowledge can be used to tailor the optimal device performance. In this paper, we report the transport properties of self-assembled monolayers derived from a series of fluorinated alkanethiols, both with and without the embedded dipole structure. Photoelectron spectroscopy and Kelvin probe force microscopy show significant work function modification from all fluorine-containing molecules compared to purely hydrocarbon thiols. However, although embedded fluorocarbons generate a smaller electrostatic effect than terminal fluorocarbons, they yield higher tunneling currents across Au/monolayer/eutectic gallium—indium junctions compared to both terminal fluorocarbon and purely hydrocarbon alkanethiols. Computational studies show that the location of the fluorine constituents modifies not only dipoles and energy levels but also molecular orbitals, enabling the presence of delocalized lowest unoccupied molecular orbital levels within the alkanethiol backbone and, thereby, the appearance of larger tunneling currents compared to other alkanethiols. Ultimately, we show that fluorinated alkanethiols and the embedded dipole architecture are both powerful tools, but they must be thoroughly analyzed for proper utilization in a device setting.

INTRODUCTION

Interfacial modification using organic monolayers is a powerful technique used to tune a wide range of surface properties. Organic monolayers can directly modify certain intrinsic properties, such as wettability[1] and chemical reactivity,[2−4] and they can also be used to modify the electrical output of devices.[5−10] A simple yet powerful tool for modifying surfaces is the attachment of molecules via self-assembly to induce surface dipoles.[11−13] Surface dipoles shift the vacuum level of their local environment, enabling work function (WF) modifications up to an electronvolt.[14] The ability to introduce dipoles of various direction and magnitude through chemical design, which can include in situ modifications through external stimuli,[15,16] affords a tunable parameter for electronic control of surfaces. These dipole effects can modify transistor transition voltages and, when used properly, can augment device output by orders of magnitude through minimizing injection barriers between materials.[17−19]

While a number of monolayers are capable of generating surface dipoles, the chemistry of the monolayers and the physical properties they induce are important to consider. Different terminal functional groups can alter surface interactions and reactivities with other materials which, in some instances, can lead to significantly diminished currents in electronic devices.[20] In the case of organic electronics, devices are often prepared by depositing active layers from solution
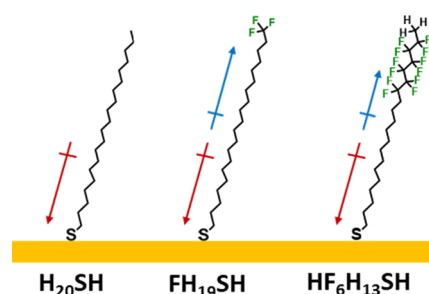
onto substrates, and changes in the surface free energy imparted by different monolayers and their terminal groups can alter the morphology and the transport properties of the deposited organic semiconductor.[21−23] To properly study and implement surface dipoles in a systematic fashion, these surface interactions must be understood and controlled.

Using embedded dipoles in self-assembled monolayers (SAMs) is a promising strategy to generate surface dipoles while maintaining control over surface properties.[24,25] The strategy behind embedded dipoles is simply to incorporate dipole-generating functional groups into the interior portions of the molecule while maintaining the chemical composition of the terminal groups. Adding dipoles along molecular termini often leads to the strongest surface dipoles, but embedded functional groups are also capable of having significant impacts (vide infra) while maintaining surface energy parameters that are crucial for interactions with active transport layers. While this approach is effective at generating large surface dipoles, embedded dipoles have been shown to generate secondary effects as well. Kovalchuk et al. have shown that the transition voltage (V_T) of charge transport can be altered in a device settings with different embedded pyrimidyl groups in p-terphenyl-based molecules.[26] Also, work by Cabarcos et al. and Taucher et al. highlight that embedded ester groups generate intramolecular electrostatic effects that modify core energy levels of the molecular constituents.[24,27] These secondary effects provide additional interest in embedded dipoles, but their appearance also highlights the complexity embedded dipoles can bring to surfaces and eventually devices, motivating careful study of embedded dipole-containing molecules to understand the full impacts they may have.

Fluorinated alkanethiols are an ideal candidate for generating embedded dipole architectures. The incorporation of fluorines in monolayers is known to generate large surface dipoles because of their electronegativity, leading to large WF modifications.[28,29] A common substitution of these atoms replaces hydrogen in C−H bonds, leading to C−F functional groups. While a number of synthetic strategies can lead to molecules possessing terminal fluorocarbons,[30] recent work has enabled fluorination solely along the backbone CH_2 groups (generating CF_2 groups) in alkanethiols, leaving the terminal CH_3 group unfluorinated and thereby generating an embedded dipole structure.[31] These embedded fluorocarbons afford the potential to generate large surface dipoles, but as discussed above, secondary effects can be generated from embedded dipole molecules. To understand both the impacts of selective fluorination and the embedded dipole in devices, we must first look at the electronic properties of the molecules themselves.

Herein, we report the impact of fluorine substitution in alkanethiols on the transport properties of SAMs derived from these molecules. We chose a subset of molecules with selective fluorination (Figure 1): a terminal fluorocarbon alkanethiol, "**$FH_{19}SH$**"; an alkanethiol with the terminal CH_3 group and fluorines embedded along the backbone, "**$HF_6H_{13}SH$**"; and a purely hydrocarbon alkanethiol control, "**$H_{20}SH$**". These molecules were incorporated into eutectic gallium−indium (EGaIn) junctions to measure the charge transport properties of these molecules as monolayers on gold. In combination with measurements of surface properties [photoelectron spectroscopy, Kelvin probe force microscopy (KPFM)] and computational studies, we observed that the selective fluorination generates significant WF modification. However, we also observed differences in the charge transport properties of

Figure 1. Diagram of the molecules studied, including an all-hydrocarbon alkanethiol ($H_{20}SH$) and two selectively fluorinated alkanethiols ($FH_{19}SH$ and $HF_6H_{13}SH$). Red arrows indicate the dipole contribution from the thiol group, and blue arrows indicate the dipole contribution from the (green) fluorine constituents, following the convention that the arrow is pointing toward the negative pole.

these molecules, which did not correlate to WF alteration or surface chemistry. We ultimately highlight that the electrostatic properties of these molecules (measured through their surface dipole effects) are not analogous to their transport properties in a device setting, and we must consider the full impact these and similar embedded dipole molecules may have on modifying device output.

■ EXPERIMENTAL SECTION

$CF_3(CH_2)_{19}SH$ (abbreviated as "**$FH_{19}SH$**") and $CH_3(CF_2)_6(CH_2)_{13}SH$ (abbreviated as "**$HF_6H_{13}SH$**") were synthesized as previously reported.[31] 1-Hexadecanethiol (abbreviated as "**$H_{16}SH$**") was purchased from Sigma-Aldrich, and 1-eicosanethiol (abbreviated as "**$H_{20}SH$**") was purchased from Alfa Aesar; both were used as received. [**Disclaimer: Any mention of commercial products is for information only; it does not imply NIST recommendation or endorsement, nor does it imply that the products mentioned are necessarily the best available for the purpose**].

Self-Assembled Monolayers. Gold evaporated on silicon was purchased from Platypus and cleaned immediately prior to use with an ultraviolet (UV)−ozone exposure for 10 min and a 60 s rinse in deionized H_2O. SAMs of all molecules were prepared inside a nitrogen glovebox ($O_2 < 5.0$ ppm) by soaking gold pieces in 10 mmol/L ethanol solution overnight, sonicating, and then rinsing with neat solvent. All molecules were electrically measured or otherwise characterized within 24 h after removal from the solvent.

Photoelectron Spectroscopy. Monolayer properties on gold were evaluated with photoelectron spectroscopy using commercial sources and detectors. Ultraviolet photoelectron spectroscopy (UPS) experiments utilized a helium source (He I, photon energy = 21.2 eV). Each measurement was averaged from three sweeps of the same spot on the sample. Measurements were taken with 25 meV steps for full scans or 10 meV steps for high-resolution scans. Linear fits at the high and low kinetic energy regions of the data were used to identify onsets of the low binding energy and cutoff regions of the spectra, respectively.

X-ray photoelectron spectroscopy (XPS) data were collected using a monochromatic Al Kα source with 10 mA emission current and 15 kV emission bias. All signals were optimized to maximize the Au $4f_{7/2}$ signal and used a 50 meV step size. Spectra were analyzed by subtracting a Shirley background and then fitting a combination of Lorentzian and Gaussian (Voigt) functions. Spin−orbit separation between the S $2p_{3/2}$ and S

$2p_{1/2}$ signals was set to 1.18 eV and that between the Au $4f_{7/2}$ and Au $4f_{5/2}$ signals was set to 3.67 eV.

Fourier Transform Infrared (FTIR) Spectroscopy. Infrared spectra were recorded with a commercial FTIR instrument with a HgCdTe (MCT) detector at 8 cm^{-1} resolution collecting 512 coadded scans. Measurements from gold on silicon substrates were acquired with a commercial 80° reflection accessory.

Microcontact Printing. Polydimethylsiloxane (PDMS) molds were prepared from Sylgard 182 silicone elastomer, poured onto silicon wafers lithographically defined with a SU-8 negative resist, and cured at 100 °C for 2 h. Once removed from the silicon wafer, PDMS contained raised micrometer-sized lines to be used in the patterned transfer of monolayers. Monolayer solutions in ethanol were drop-cast onto ≈1 cm × 1 cm pieces of the PDMS mold and allowed to dry. Finally, the monolayer-soaked PDMS stamp was contacted to cleaned gold surfaces for <30 s. No further cleaning of the monolayer on gold pieces was performed to prevent diffusion of molecules into bare gold regions.

Kelvin Probe Force Microscopy. KPFM measurements were carried out using a Dimension 5000 microscope with Nanoscope V electronics (Bruker, Santa Barbara, USA). Pt/Ir-coated silicon tips (Nano World Holding AG, Neuchâtel, Switzerland) have a typical first resonance frequency of around 75 kHz and a force constant of 3 N/m. In this work, KPFM was performed in LiftMode, where the first trace recorded topographical data in the tapping mode, then the tip was held at a constant separation from the local surface topography (here 10 nm), and the second trace recorded surface potential.

Electrical Measurements. Transport measurements of the monolayers were accomplished using EGaIn top contacts with device structure consisting of Au/SAM/EGaIn. EGaIn was purchased from Sigma-Aldrich (75.5% Ga, 24.5% In by mass) and used as received. The material was used to form conical tips by dispensing 0.2 μL from a Hamilton 701SN 10 μL syringe, contacting the dispensed liquid with a bare gold surface, and retracting the syringe until cleavage of EGaIn in the syringe from the EGaIn adhered to the gold.[32] The resulting tips were commonly ≈20 μm in diameter. DC current−voltage (I−V) sweeps were performed by contacting the EGaIn tip in the syringe with monolayers on gold, using EGaIn as the top contact and gold substrate as the bottom contact, and sweeping the voltage from ±0.5 V. Each electrical junction was optically recorded and measured to extract current density (J) values.
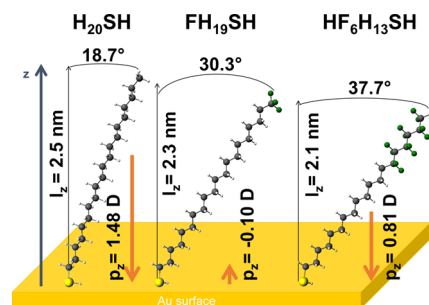
Computational Details. The dipole moments and molecular orbitals were obtained with the ADF program, version 2016.[33−35] The triple zeta basis set[36] and the B3LYP functional[37] with the Grimme D3-dispersion correction[38] were used. An all-electron calculation was performed during the geometry optimization. Using angles determined from previous ellipsometry measurements[12] and calculated molecular lengths, the angles of the SAM molecules were kept constant during the optimization to ensure that the alkyl chains remained in the trans-extended zigzag structure.

■ RESULTS AND DISCUSSION

Surface Dipole Calculations. The molecules selected for this study present different dipole magnitudes that can generate a range of WFs from the metal surfaces to which they are attached. For each of these molecules, there are several components which impact the surface dipole and, subsequently, the surface WF. Predominantly, the fluorinated SAMs will have

strong contributions from the thiol−gold bond and the fluorine atoms. The Au−S bond will pull electron density toward the substrate and decrease the surface WF (as indicated with the red dipole arrow in Figure 1, following the convention that the arrow is pointing toward the negative pole), and the electronegative fluorine atoms will draw electron density away from the metal surface and increase the surface WF (as indicated by the blue dipole arrow).

Figure 2 contains the calculated total dipole moment of the three studied SAM molecules. The molecular chain length is

Figure 2. Calculated monolayer lengths (l_z) and total dipole moments (p_z) perpendicular to the substrate (z direction) of the three SAM molecules (left to right: $H_{20}SH$, $FH_{19}SH$, and $HF_6H_{13}SH$) incorporating their tilt angle relative to surface normal. Dipole arrows (orange) follow the convention where the arrow is pointing toward the negative pole. Yellow atoms represent sulfur, green atoms represent fluorine, gray atoms represent carbon, and white atoms represent hydrogen. Dipole moments are presented in Debye (also in C·m in the text).

about 2.6 nm measured from the sulfur atom to the most distant hydrogen or fluorine atom along the chain for all three molecules. However, the monolayers have varying tilt angles with respect to the gold substrate, and vertical film thicknesses between 2.5 and 2.1 nm for these SAMs are reported.[12] Taking this tilt into account, we can determine the dipole moment perpendicular to the surface, which will be most relevant to devices where transport occurs in that direction. Our calculations yield that both $H_{20}SH$ and $HF_6H_{13}SH$ have net positive dipole moments (toward the surface) of 4.94×10^{-30} C·m (1.48 D) and 2.70×10^{-30} C·m (0.81 D), respectively. $FH_{19}SH$, on the other hand, has a small net dipole moment in the opposite direction (away from the surface) of -3.34×10^{-31} C·m (−0.10 D). The reason for this is the thiol head group that introduces a dipole moment of about 5.00×10^{-30} C·m (1.50 D), whereas the CF$_3$-terminating group has a dipole moment of -5.47×10^{-30} C·m (−1.64 D), thus giving a near cancelation of the total dipole moment (see the Supporting Information). The wide range in calculated monolayer dipoles suggests that these molecules are an ideal set to consider the impact of dipoles from selective fluorination on WF changes and charge transport at the metal−organic interface.

It should be noted that the presence of any adsorbate on a metal surface will alter the WF by changing the local electron density at the surface. Specific causes for this effect include Coulomb repulsion and Pauli exclusion effects.[39,40] In addition, the local dipole of the Au−S bond has been the subject of vigorous debate. Previous XPS studies of aliphatic SAMs suggest that the contributions from the bond toward the surface dipole can range from near zero (±0.05 eV) up to several tenths of an electronvolt.[27,41] Our dipole calculations above do not consider contributions from the Au−S bond. However, the

molecules in this study contain nearly identical Au−S bonding as observed through the XPS Au−S peak location (Supporting Information) and are similar in chain length and other monolayer properties, indicating that any resulting change in WF from these SAMs will be dominated by the fluorination differences.

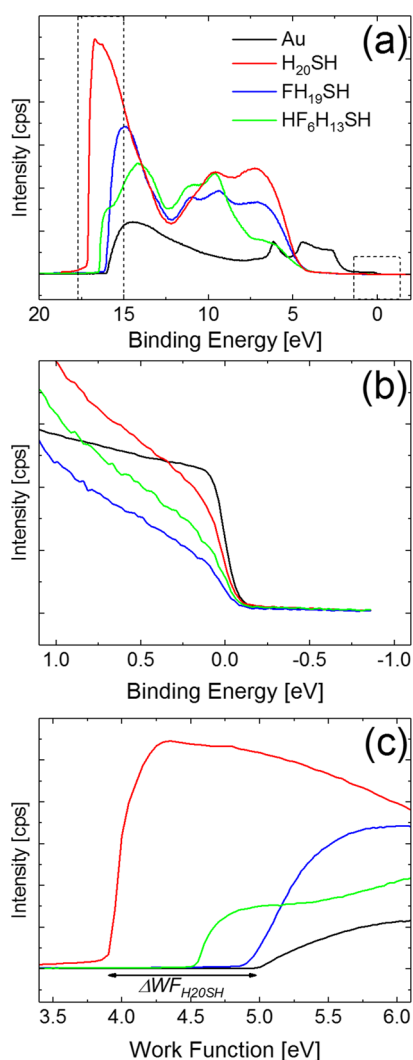**Monolayer Formation and Gold WF Modification.** Alkanethiols tend to form well-packed monolayers on gold,[42] and in spite of the substitution of fluorine atoms, the molecules in this study possess 20-carbon long backbones that are designed to promote highly ordered SAMs. Once assembled as SAMs on gold surfaces, we do observe slight differences in packing density between the molecules, but our characterization of functionalized gold surfaces by XPS, FTIR, and contact angle (see the Supporting Information) indicates the presence of high-quality monolayer packing for all molecules, consistent with previous reports of similar molecules.[12,31]

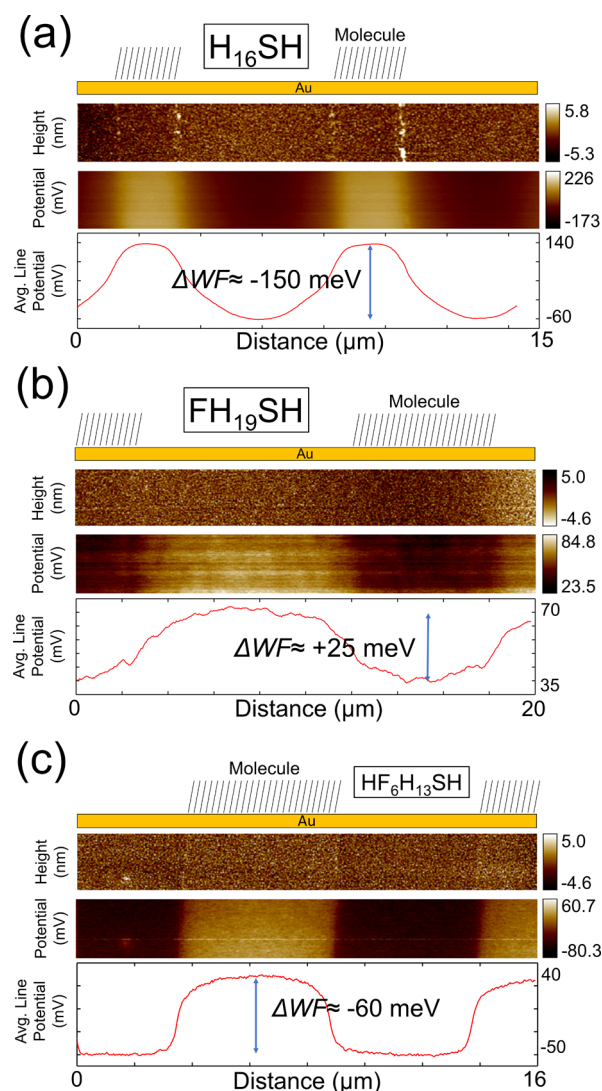The surface dipoles from the selective fluorination are experimentally observed through the UPS characterization of the SAMs (Figure 3). Because the Fermi edge for all monolayers is identical (Figure 3b), the WF can be observed through the shifts in the secondary electron cutoff region (Figure 3c), which is plotted to directly show the WFs of the SAMs. The WF of bare gold surfaces has been measured as $WF_{Au} = (5.0 \pm 0.1)$ eV, where the value after "±" denotes one standard deviation. By comparing this to SAM-functionalized surfaces, we see that SAMs of $H_{20}SH$ exhibit a decrease in WF ($WF_{H_{20}SH} = (3.8 \pm 0.1)$ eV) in agreement with prior reports.[43,44] As suggested, fluorination will increase the WF from this point, and we measure that the two fluorinated monolayers on gold have WF greater than $H_{20}SH$ ($WF_{FH_{19}SH} = (4.9 \pm 0.1)$ eV, $WF_{HF_6H_{13}SH} = (4.5 \pm 0.1)$ eV). These WF modifications match previously reported values of similar molecules[12,41,43] and also correlate to the trend of calculated surface dipoles (vide supra). In addition, the WF difference of ≈1.1 eV between the CH_3-terminated $H_{20}SH$ and the CF_3-terminated $FH_{19}SH$ matches literature reports of surface potential differences because of fluorination of the alkanethiol terminal group.[45] Finally, this result highlights that the $HF_6H_{13}SH$ SAM and its embedded dipole from the fluorocarbons have a significant contribution toward the total surface dipole (≈0.7 eV difference in WF from $H_{20}SH$).

Kelvin Probe Force Microscopy. To further highlight the WF modification from these molecules, we used KPFM to measure the change in WF from patterned microcontact-printed (μCP) monolayers (Figure 4). KPFM, which utilizes a nanometer-sized cantilever for measuring surface potential, offers the ability to collect local surface measurements at a smaller scale than is typically offered with UPS. In combination with the capability of μCP to pattern micrometer-sized strips of monolayers while leaving adjacent regions of bare gold exposed, this technique allows for direct measurement of WF modification imparted by the monolayers. For these measurements, we utilized a slightly shorter alkanethiol monolayer, $H_{16}SH$, alongside our 20-carbon fluorinated alkanethiols. The shorter $H_{16}SH$ exhibits a slight change in WF modification compared to $H_{20}SH$ when measured as a solution-soaked SAM in UPS ($WF_{H_{16}SH} = (4.2 \pm 0.1)$ eV; see the Supporting Information), which correlates to its slightly diminished dipole moment (Supporting Information), but otherwise, it is an analogous hydrocarbon thiol to its longer counterpart in these measurements. In addition, the stamps used to print monolayers possessed a range of widths (2−10 μm), and, while representative images are shown here, differences in widths of the monolayer regions have no impact on the obtained results.

For these μCP monolayers, $H_{16}SH$ exhibits the largest negative shift in the WF, while the fluorinated monolayers induce smaller WF changes (increased WF) in agreement with the UPS data. In this instance, the shift for the $FH_{19}SH$ monolayer is slightly positive, which has been seen previously with data obtained from other terminally fluorinated monolayers,[43] though both this and the UPS result yield ΔWF values very close to zero. The KPFM results match the UPS-measured WF trend in agreement with literature reports of strong correlation between UPS and KPFM.[24] In our measurements, we observed a smaller WF change from the molecules on the KPFM-measured sample than on the UPS-measured samples. The reduced impact is likely due to a number of factors. First, while monolayers used for UPS were soaked overnight for optimized packing and density, the short equilibration time used to form the μCP monolayers (<30 s) leads to lower
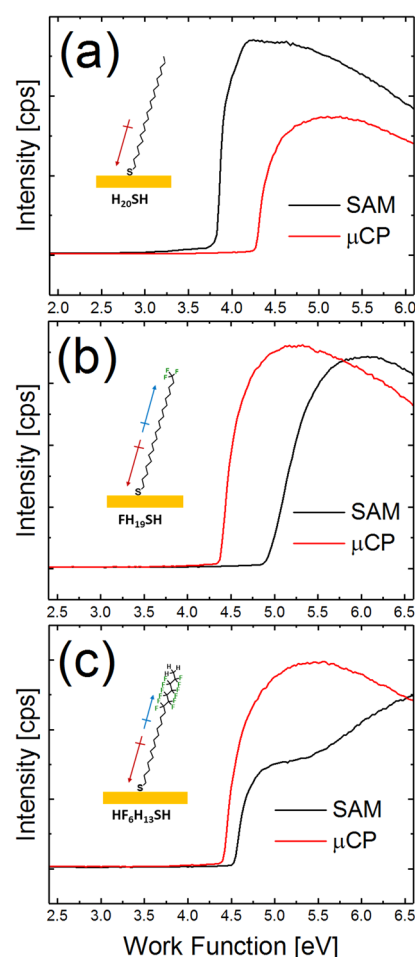

Figure 3. (a) UPS spectra for fluorinated alkanethiol SAMs on gold (black lines: bare Au, red lines: $H_{20}SH$, blue lines: $FH_{19}SH$, green lines: $HF_6H_{13}SH$). Highlighted regions are expanded to show the (b) Fermi edge of all surfaces, and (c) secondary electron cutoff region, plotted as WF and presenting ΔWF relative to the bare gold surface.

Figure 4. KPFM results for fluorinated alkanethiols patterned on gold using μCP from PDMS stamps for (a) $H_{16}SH$, (b) $FH_{19}SH$, and (c) $HF_6H_{13}SH$. All figures show, from top to bottom: molecule location, measured height, measured surface potential, and average line profile of the surface potential. The surface potential in monolayer regions and potential in bare gold regions are used to calculate the WF values shown. All ΔWF values contain an error bar of ± 10 meV.

Figure 5. UPS spectra for solution-soaked self-assembled monolayers (SAMs; black line) and unpatterned, μCP monolayers (red line), highlighting the WF difference caused by different monolayer densities from the preparation techniques. Unpatterned μCP monolayers are used here to prevent convoluted results from alternating Au and monolayer regions. (a) $H_{20}SH$ monolayers, where higher density decreases WF; (b) $FH_{19}SH$ monolayers, where higher density from more fluorines increases WF; and (c) $HF_6H_{13}SH$ monolayers, where higher density from more fluorines increases WF.
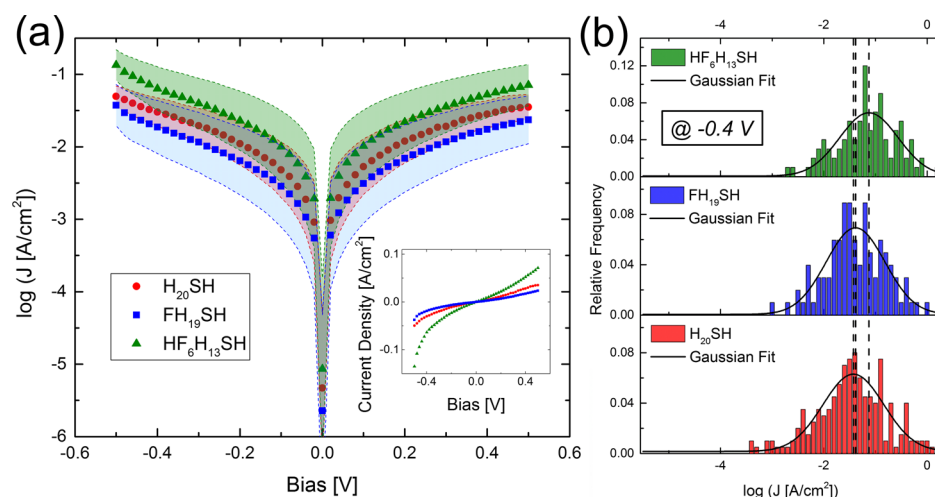
molecular density. Such a short time for the stamp to be in contact with the gold film is necessary to prevent contamination of the monolayer into the bare gold regions, but direct comparison of solution-soaked monolayers and μCP monolayers yields different WF shifts because of this density difference. This is experimentally verified by comparing solution-soaked SAMs and unpatterned μCP films (molecules printed in large area, $\approx$1 cm × 1 cm sheets), which confirms different WF shifts (Figure 5). Second, our KPFM measurement is achieved using a setup in ambient conditions. This allows for quick measurements on freshly prepared films; however, the ambient conditions can allow the presence of a water meniscus or the adsorption of adventitious carbon to minimize the measured change in surface potential.

Au/SAM/EGaIn Device Measurements. Having shown the impact of selective fluorination and embedded fluorine dipole on surface WF, we next turn our focus to charge transport through these monolayers. We selected molecules

with identical length for this study ($FH_{19}SH$, $HF_6H_{13}SH$, and $H_{20}SH$), and while small differences in tilt angle were observed because of slight differences in monolayer packing (Supporting Information), the through-bond tunneling length for these molecules is identical and should dominate the transport. The monolayers were incorporated into electrical junctions using EGaIn to form a top contact. While numerous methods exist for incorporating organic-based monolayers into molecular junctions,[46−50] EGaIn top contact devices afford the ability for facile and repeatable measurements in ambient environment.[20,32] EGaIn top contacts were formed by contacting a drop from a syringe onto a bare gold surface and retracting the syringe, causing a severance in the center of the eutectic liquid. Because of the non-Newtonian EGaIn properties, this severance resulted in the formation of approximately 20 μm diameter conical tips that were used as an electrical top contact to measure the charge transport properties of the monolayer/ Au substrate. We used a manipulator stage with sub-micrometer resolution to create electrical contact between EGaIn and the monolayer (see the Supporting Information for

Figure 6. Electrical measurements from 100+ EGaIn/monolayer/Au devices for each monolayer. (a) Geometric average log|J| plots for all electrical data for SAMs derived from $H_{20}SH$ (red circles), $FH_{19}SH$ (blue squares), and $HF_6H_{13}SH$ (green triangles). Colored regions surrounding the points represent one standard deviation. Inset: Geometric average J vs V plot. (b) Histograms of device currents at −0.4 V for EGaIn/monolayer/Au devices, fitted with Gaussian distributions. Dotted lines correspond to maximum log|J| location of each Gaussian.

the optical device image). While the junctions were sometimes measurable to ±2.0 V before electrical breakdown, the most consistent measurements were obtained using a ±0.5 V window. Over 100 measurements were obtained across multiple monolayer/Au substrates to gain a statistical representation of the device properties. To account for differences in tip sizes between measurements, the size of each junction was optically measured and the current normalized to the junction area. Furthermore, to prevent contributions from the oxidation of EGaIn,[51] we formed a new EGaIn tip after every five measurements. Careful controls for tip size, tip oxidation, and other device variations are discussed in detail in the Supporting Information to ensure that the EGaIn data are an accurate measurement of charge transport through these molecular layers.

Figure 6 shows the results from our EGaIn measurements. These monolayers express primarily tunneling characteristics (Figure 6a), which is expected given that they are primarily ≈2 nm long aliphatic chains. To gain statistical representations of our measurements, we selected the current densities measured at −0.4 V bias and plotted a histogram of the output for all 100+ devices (Figure 6b). These histograms exhibit log−normal Gaussian distributions that are common for molecular electronic junctions.[52] The results of similar histogram fits for different biases are shown in Table 1.

From the log−normal fits obtained from the histograms, we can see that devices formed using $HF_6H_{13}SH$ SAMs have a higher log |J| when compared to those formed using $H_{20}SH$ and

FH$_{19}$SH SAMs (as confirmed by t-test with 99% confidence), whereas $H_{20}SH$ and $FH_{19}SH$ SAM devices exhibit statistically equivalent current densities. Such an outcome is slightly unexpected because the barrier for tunneling transport across the metal−molecule junction should be correlated to the alignment of the Fermi level and the molecular orbitals,[53] and we would expect the charge transport to be dominated by the shifting of vacuum level/energy levels as indicated by the change in WF. From this model, we would expect the largest current density to occur through the $H_{20}SH$ monolayer (where energy levels and therefore barriers are lowered by the large decrease in WF) and the smallest current density through $FH_{19}SH$. This expectation failed to match our results, indicating that a different phenomenon is dominating the charge transport.

Impact from Interfaces. Interfaces play an important role in this study as the barrier at either interface could dominate the charge transport through the molecular layer. Previous reports of aromatic molecules with fluorine-capped monolayers have shown significant contact resistance changes in EGaIn junctions with the fluorine constituent causing as much as a 30% reduction in the measured current density.[20] Herein lies the original intention of embedding dipoles in these molecules: to maintain the interface while adding dipoles into the noninterfacial regions of the molecules. $H_{20}SH$ and $FH_{19}SH$ are the best comparison of contact resistance in this study, with only the terminal group differing between the molecules. However, the electrical data obtained from these junctions is indistinguishable, indicating that there is no significant impact from the CF_3- versus CH_3- terminus in these measurements. Furthermore, despite maintaining the terminal CH_3 group for $H_{20}SH$ and $HF_6H_{13}SH$ SAMs, we obtained statistically different current densities. Inelastic electron tunneling spectroscopy in literature experiments observed a similar lack of dependence with nonembedded fluorine substitution in aliphatic molecules, suggesting that tunneling is insensitive to fluorine substitution for the molecules in question.[54] The significant >2 nm tunneling barrier from the aliphatic chains likely dominated the measured charge transport, effectively overriding any differences in the contact resistance.

Table 1. Gaussian Fits for EGaIn/SAM/Au log|J| Histograms at Various Biases

	max log|J| (A/cm^2)		
Bias (V)	$H_{20}SH$	$FH_{19}SH$	$HF_6H_{13}SH$
−0.4	−1.4 ± 0.5	−1.4 ± 0.6	−1.1 ± 0.6
−0.2	−1.9 ± 0.6	−1.8 ± 0.6	−1.6 ± 0.6
−0.1	−2.2 ± 0.6	−2.2 ± 0.6	−1.9 ± 0.6
+0.1	−2.2 ± 0.6	−2.2 ± 0.6	−1.9 ± 0.6
+0.2	−1.8 ± 0.6	−1.8 ± 0.5	−1.6 ± 0.6
+0.4	−1.4 ± 0.6	−1.4 ± 0.6	−1.2 ± 0.6

Table 2. Calculated Frontier Orbitals, Ionization Potential, and HOMO−LUMO Gap (E_g) Values for SAMs Derived from the Indicated Thiols[a]

molecule	HOMO−1 [eV]	HOMO [eV]	LUMO [eV]	LUMO+1 [eV]	vertical ionization potential (IP) [eV]	HOMO−LUMO gap (E_g) [eV]
$H_{20}SH$	−7.55	−6.43	−0.43	0.27	8.02	6.00
$HF_6H_{13}SH$	−8.04	−6.48	−0.69	−0.54	8.38	5.79
$FH_{19}SH$	−7.73	−6.45	−0.44	0.09	8.15	6.01

[a]Frontier Orbital values were internally referenced to the calculation, thus the zero point is common though externally unreferenced. Ionization potential defines the absolute reference point for these energy levels.
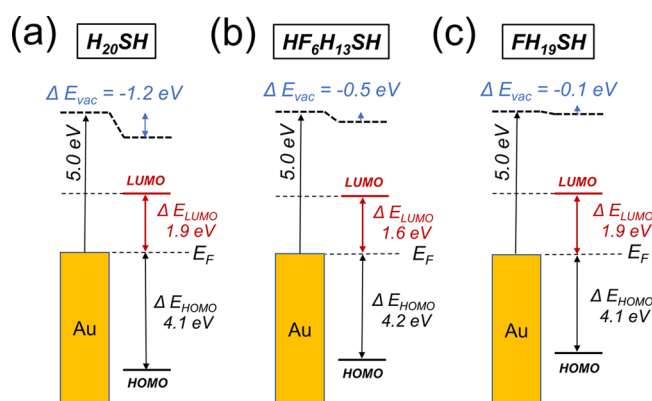
Fluorination Effects on Energy Levels. With no observed correlation between terminal functionality and current density, we look to other sources for the observed current density trends. Fluorination is known to modify the highest occupied molecular orbital (HOMO) and lowest unoccupied molecular orbital (LUMO) levels of organic materials and is used as a common method to lower energy levels by as much as 1 eV.[30] To observe any similar energy level modification in our molecules, we calculated the energy levels and molecular orbitals for the fluorinated alkanethiols using gas-phase density functional theory (DFT) (Table 2). First, the calculations showed shifts in the HOMO and LUMO energy levels for these molecules relative to each other, with the largest shift seen in the $HF_6H_{13}SH$ LUMO at ≈0.3 eV lower than the LUMOs for $H_{20}SH$ and $FH_{19}SH$, respectively, once the different HOMO−LUMO gaps are taken into account. Because the LUMO is expected to dictate the tunneling barrier in these molecules,[55] such a shift can generate different tunneling barriers and therefore different current densities across our devices.

Figure 7 expresses this point by presenting band diagrams and tunneling barriers for the molecules, incorporating the

Figure 7. Band diagrams for (a) $H_{20}SH$, (b) $HF_6H_{13}SH$, and (c) $FH_{19}SH$. Diagram based on experimentally determined HOMO levels from UPS (ΔE_{HOMO}), measured surface dipoles used to estimate the change in vacuum level (ΔE_{vac}, with the assumption that $\Delta WF = \Delta E_{vac}$), and measured $WF_{Au} = 5.0$ eV. ΔE_{LUMO} is determined using the computed HOMO−LUMO gap in the main text and represents the tunneling barrier height for transport from Au into the molecule. All values have ±0.1 eV error.

experimentally determined HOMO levels, ΔE_{vac} (from ΔWF and the UPS measurements), and the calculated HOMO−LUMO gap. To construct the band diagram, we started with the WF of clean gold ($WF_{Au} = (5.0 \pm 0.1)$ eV) as measured by UPS. The shift in WF with the addition of the SAMs leads to a change in the vacuum level as indicated at the top of each band diagram. The HOMO energy level for all

three molecules was determined from the UPS data (Figure 3a) and appears pinned at 4.1 to 4.2 eV below the Fermi level, likely because of similar Au−S interfacial bonding. The LUMO levels were determined by using the calculated HOMO−LUMO gap (E_g). The LUMO level offset from the gold becomes the injection barrier for transport and ranges from 1.6 to 1.9 eV, with a slightly smaller barrier height obtained for $HF_6H_{13}SH$ because of the aforementioned lowered LUMO. Band diagrams using the calculated HOMO and LUMO energies and ionization potential values are shown in the Supporting Information and follow the same trend with slightly higher barrier heights (2.4 −3.0 eV). The lower barrier height from $HF_6H_{13}SH$ is in agreement with the higher current density observed for the EGaIn junctions incorporating $HF_6H_{13}SH$, providing a possible explanation for the results from our EGaIn measurements.
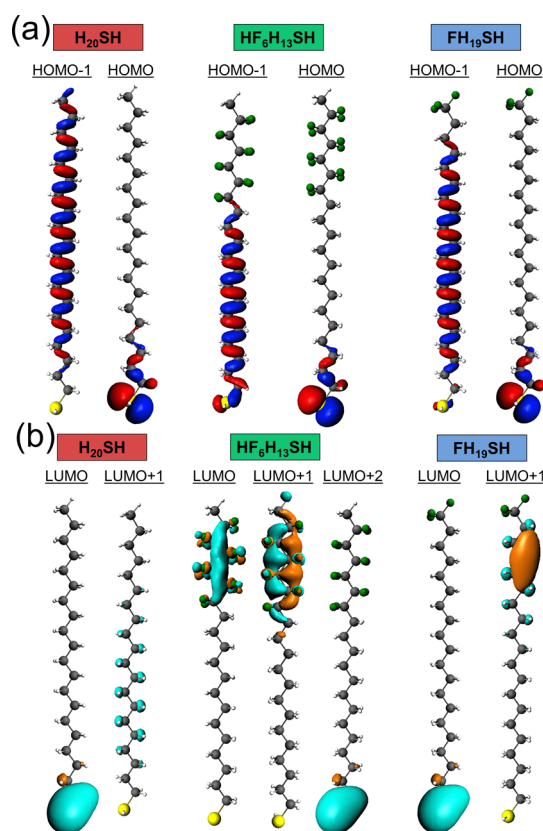
In addition, examining the energy levels beyond the LUMO gives an indication of whether there are additional energetically accessible tunneling states. The molecular orbitals are shown in Figure 8 and Table 2, while the relative energy scale of the orbitals is contained in the Supporting Information. Both $H_{20}SH$ and $FH_{19}SH$ have an energy barrier greater than 0.5 eV between the LUMO and the next accessible MO, LUMO+1. However, $HF_6H_{13}SH$ has the LUMO, LUMO+1, and LUMO+2 all closely grouped in energy, providing more accessible molecular orbitals for tunneling. Ultimately, there is strong correlation between the impact of selective fluorination on orbital energy levels and the higher current density observed for the EGaIn junctions incorporating $HF_6H_{13}SH$, providing a possible explanation for the results from our EGaIn measurements.

Fluorination Effects on Molecular Orbitals. While the band diagram and injection barriers correlate with our experimental results, the DFT-calculated molecular orbitals for these molecules (Figure 8) also highlight properties that can explain our experimental results. The observed HOMO is very similar for all three molecules and correlates well with HOMO levels being nearly identical in terms of energy. The HOMO−1 electron distributions are still similar, with the fluorine shifting the HOMO−1 to lower energies for $FH_{19}SH$ and $HF_6H_{13}SH$. However, as asserted above, transport across these molecules is LUMO-mediated, and there are substantial differences for the LUMOs for these three molecules. Whereas the electron density for both the HOMO and the LUMO exists on the thiol (bottom) portion of the molecule for $H_{20}SH$ and $FH_{19}SH$, the LUMO for $HF_6H_{13}SH$ is delocalized across the fluorinated (top) portion of the molecule, which accounts for about one-third the length of the molecule. This shape is similar in the LUMO+1 of $HF_6H_{13}SH$, and finally, the LUMO+2 is localized on the thiol portion as with the $H_{20}SH$ and $FH_{19}SH$ HOMO and LUMO. This observation is significant because the delocalized LUMO and LUMO+1 of $HF_6H_{13}SH$ can reduce the effective tunneling distance across the molecule, thereby

Figure 8. DFT-calculated molecular orbitals for (A) HOMO−1 and HOMO orbitals and (B) LUMO, LUMO1, and LUMO+2 orbitals (lattermost as indicated). From left to right, orbitals correspond to $H_{20}SH$, $HF_6H_{13}SH$, and $FH_{19}SH$. Thiol portion of the chain (yellow circles = sulfur) on bottom of images and fluorinated sections of applicable chains (green circles = fluorine) on top.

increasing the measured tunneling current.[56] Our tunneling barrier is multiple electronvolts in height and our measurements ranged from −0.5 V to +0.5 V, so we do not suggest occupation of this orbital during transport. However, the calculations presented here highlight the unique molecular orbital nature generated by the fluorocarbon segment of the $HF_6H_{13}SH$ molecule and, specifically, the potential for delocalized transport across the molecule. Given the significant size of this segment, we expect this facilitates tunneling in the $HF_6H_{13}SH$ SAM through a means not present in the $FH_{19}SH$ and $H_{20}SH$ SAMs.

There is a broader significance to be stated from this work: the chemical makeup of interfacial modifying layers must be taken into account to fully understand their impact in devices. Again, the intention behind "embedding" dipoles is to generate large surface dipoles while removing any influence from the dipole-generating constituents on other device properties. However, the embedded fluorines in the $HF_6H_{13}SH$ molecule gave rise to significant secondary consequences, including different intermolecular interactions which slightly decrease monolayer density and, most relevant to the results presented here, modification of transport properties through orbitals delocalized along the embedded fluorines. We still suggest that this embedded structure holds promise as surface interactions are important to control. In the case of shorter molecules, contact resistance will have a much more significant impact on transport than the 20-carbon alkanethiol molecules studied here. Also, the formation and morphology of organic

semiconductors deposited on SAMs are still dependent on surface energy. However, even with analogous surface interactions, embedded dipole molecules must not be utilized simply and haphazardly. Careful study of their molecular properties and, in the case of electrical devices, transport properties are necessary such that the benefits these molecules might have on the device output are understood and correctly assigned.

CONCLUSIONS

In conclusion, we have prepared and characterized SAMs generated from selectively fluorinated alkanethiols, containing both embedded and nonembedded fluorocarbons, to test the effects of fluorination and embedded dipoles on transport properties across the monolayer. We find that fluorine location in the molecule has a measurable impact on the WF modification of the surface, but that embedded fluorocarbons are still capable of generating large surface dipoles. When these SAMs are measured as tunneling junctions, we find no direct correlation between surface dipole or gold WF modification and device current density. We also observe a similar lack of connection between the terminal functional group ($CH_3−$ vs $CF_3−$) and the measured output. We attribute the lack of interfacial impacts to the significant length of the tunneling barrier and further attribute the currents measured through the molecules to the DFT-calculated molecular orbitals. The energetically lower LUMO positions calculated for $HF_6H_{13}SH$ may cause a lower tunneling barrier, and the LUMO/LUMO+1 of $HF_6H_{13}SH$ also has a much broader electron density component, facilitating shorter tunneling distance and increasing the current density through these junctions. This study overall highlights the importance in measuring and considering all molecular properties, even when embedding dipoles, to properly understand the impacts of monolayers for use in generating surface dipoles.

ASSOCIATED CONTENT

Ⓢ Supporting Information

The Supporting Information is available free of charge on the ACS Publications website at DOI: 10.1021/acs.jpcc.7b11892.

XPS and additional UPS data; contact angle measurements; FTIR data; analysis of EGaIn setup, tip effects, and electrical data; additional computational data; and alternate band diagram (PDF)

AUTHOR INFORMATION

Corresponding Authors

*E-mail: robert.bruce@nist.gov (R.C.B.).

*E-mail: christina.hacker@nist.gov (C.A.H.).

ORCID Ⓞ

Robert C. Bruce: 0000-0002-4542-7345

Anja Förster: 0000-0002-2203-8662

T. Randall Lee: 0000-0001-9584-8861

Notes

The authors declare no competing financial interest.

ACKNOWLEDGMENTS

■ REFERENCES

(1) Chinwangso, P.; Lee, H. J.; Jamison, A. C.; Marquez, M. D.; Park, C. S.; Lee, T. R. Structure, Wettability, and Thermal Stability of Organic Thin-Films on Gold Generated from the Molecular Self-Assembly of Unsymmetrical Oligo(ethylene Glycol) Spiroalkanedithiols. *Langmuir* **2017**, *33*, 1751−1762.

(2) Adamson, K.; Spain, E.; Prendergast, U.; Moran, N.; Forster, R. J.; Keyes, T. E. Peptide-Mediated Platelet Capture at Gold Micropore Arrays. *ACS Appl. Mater. Interfaces* **2016**, *8*, 32189−32201.

(3) Ono, T.; Oe, T.; Kanai, Y.; Ikuta, T.; Ohno, Y.; Maehashi, K.; Inoue, K.; Watanabe, Y.; Nakakita, S.-i.; Suzuki, Y.; et al. Glycan-Functionalized Graphene-FETs toward Selective Detection of Human-Infectious Avian Influenza Virus. *Jpn. J. Appl. Phys.* **2017**, *56*, 030302.

(4) Park, H.; Afzali, A.; Han, S.-J.; Tulevski, G. S.; Franklin, A. D.; Tersoff, J.; Hannon, J. B.; Haensch, W. High-Density Integration of Carbon Nanotubes via Chemical Self-Assembly. *Nat. Nanotechnol.* **2012**, *7*, 787−791.

(5) Bruce, R. C.; Wang, R.; Rawson, J.; Therien, M. J.; You, W. Valence Band Dependent Charge Transport in Bulk Molecular Electronic Devices Incorporating Highly Conjugated Multi-[(Porphinato)Metal] Oligomers. *J. Am. Chem. Soc.* **2016**, *138*, 2078−2081.

(6) Haj-Yahia, A.-E.; Yaffe, O.; Bendikov, T.; Cohen, H.; Feldman, Y.; Vilan, A.; Cahen, D. Substituent Variation Drives Metal/Monolayer/Semiconductor Junctions from Strongly Rectifying to Ohmic Behavior. *Adv. Mater.* **2013**, *25*, 702−706.

(7) Campbell, I. H.; Rubin, S.; Zawodzinski, T. A.; Kress, J. D.; Martin, R. L.; Smith, D. L.; Barashkov, N. N.; Ferraris, J. P. Controlling Schottky Energy Barriers in Organic Electronic Devices Using Self-Assembled Monolayers. *Phys. Rev. B: Condens. Matter Mater. Phys.* **1996**, *54*, R14321−R14324.

(8) Salinas, M.; Jäger, C. M.; Amin, A. Y.; Dral, P. O.; Meyer-Friedrichsen, T.; Hirsch, A.; Clark, T.; Halik, M. The Relationship between Threshold Voltage and Dipolar Character of Self-Assembled Monolayers in Organic Thin-Film Transistors. *J. Am. Chem. Soc.* **2012**, *134*, 12648−12652.

(9) Margapoti, E.; Li, J.; Ceylan, Ö.; Seifert, M.; Nisic, F.; Le Anh, T.; Meggendorfer, F.; Dragonetti, C.; Palma, C.-A.; Barth, J. V.; et al. A 2D Semiconductor-Self-Assembled Monolayer Photoswitchable Diode. *Adv. Mater.* **2015**, *27*, 1426−1431.

(10) Pookpanratana, S.; Zhu, H.; Bittle, E. G.; Natoli, S. N.; Ren, T.; Richter, C. A.; Li, Q.; Hacker, C. A. Non-Volatile Memory Devices with Redox-Active Diruthenium Molecular Compound. *J. Phys.: Condens. Matter* **2016**, *28*, 094009.

(11) Heimel, G.; Romaner, L.; Zojer, E.; Bredas, J.-L. The Interface Energetics of Self-Assembled Monolayers on Metals. *Acc. Chem. Res.* **2008**, *41*, 721−729.

(12) Lee, H. J.; Jamison, A. C.; Lee, T. R. Surface Dipoles: A Growing Body of Evidence Supports Their Impact and Importance. *Acc. Chem. Res.* **2015**, *48*, 3007−3015.

(13) Ellison, D. J.; Lee, B.; Podzorov, V.; Frisbie, C. D. Surface Potential Mapping of SAM-Functionalized Organic Semiconductors by Kelvin Probe Force Microscopy. *Adv. Mater.* **2011**, *23*, 502−507.

(14) Kim, J.; Rim, Y. S.; Liu, Y.; Serino, A. C.; Thomas, J. C.; Chen, H.; Yang, Y.; Weiss, P. S. Interface Control in Organic Electronics Using Mixed Monolayers of Carboranethiol Isomers. *Nano Lett.* **2014**, *14*, 2946−2951.

(15) Bartucci, M. A.; Florián, J.; Ciszek, J. W. Spectroscopic Evidence of Work Function Alterations Due to Photoswitchable Monolayers on Gold Surfaces. *J. Phys. Chem. C* **2013**, *117*, 19471−19476.

(16) Masillamani, A. M.; Osella, S.; Liscio, A.; Fenwick, O.; Reinders, F.; Mayor, M.; Palermo, V.; Cornil, J.; Samorì, P. Light-Induced Reversible Modification of the Work Function of a New Perfluorinated Biphenyl Azobenzene Chemisorbed on Au (111). *Nanoscale* **2014**, *6*, 8969−8977.

(17) de Boer, B.; Hadipour, A.; Mandoc, M. M.; van Woudenbergh, T.; Blom, P. W. M. Tuning of Metal Work Functions with Self-Assembled Monolayer. *Adv. Mater.* **2005**, *17*, 621−625.

(18) Kobayashi, S.; Nishikawa, T.; Takenobu, T.; Mori, S.; Shimoda, T.; Mitani, T.; Shimotani, H.; Yoshimoto, N.; Ogawa, S.; Iwasa, Y. Control of Carrier Density by Self-Assembled Monolayers in Organic Field-Effect Transistors. *Nat. Mater.* **2004**, *3*, 317−322.

(19) Haick, H.; Pelz, J. P.; Ligonzo, T.; Ambrico, M.; Cahen, D.; Cai, W.; Marginean, C.; Tivarus, C.; Tung, R. T. Controlling Au/n-GaAs Junctions by Partial Molecular Monolayers. *Phys. Status Solidi A* **2006**, *203*, 3438−3451.

(20) Liao, K.-C.; Bowers, C. M.; Yoon, H. J.; Whitesides, G. M. Fluorination, and Tunneling across Molecular Junctions. *J. Am. Chem. Soc.* **2015**, *137*, 3852−3858.

(21) Asadi, K.; Wu, Y.; Gholamrezaie, F.; Rudolf, P.; Blom, P. W. M. Single-Layer Pentacene Field-Effect Transistors Using Electrodes Modified With Self-Assembled Monolayers. *Adv. Mater.* **2009**, *21*, 4109−4114.

(22) Ito, Y.; Virkar, A. A.; Mannsfeld, S.; Oh, J. H.; Toney, M.; Locklin, J.; Bao, Z. Crystalline Ultrasmooth Self-Assembled Monolayers of Alkylsilanes for Organic Field-Effect Transistors. *J. Am. Chem. Soc.* **2009**, *131*, 9396−9404.

(23) Bock, C.; Pham, D. V.; Kunze, U.; Käfer, D.; Witte, G.; Wöll, C. Improved Morphology and Charge Carrier Injection in Pentacene Field-Effect Transistors with Thiol-Treated Electrodes. *J. Appl. Phys.* **2006**, *100*, 114517.

(24) Cabarcos, O. M.; Schuster, S.; Hehn, I.; Zhang, P. P.; Maitani, M. M.; Sullivan, N.; Giguère, J.-B.; Morin, J.-F.; Weiss, P. S.; Zojer, E.; Zharnikov, M.; et al. Effects of Embedded Dipole Layers on Electrostatic Properties of Alkanethiolate Self-Assembled Monolayers. *J. Phys. Chem. C* **2017**, *121*, 15815−15830.

(25) Kovalchuk, A.; Egger, D. A.; Abu-Husein, T.; Zojer, E.; Terfort, A.; Chiechi, R. C. Dipole-Induced Asymmetric Conduction in Tunneling Junctions Comprising Self-Assembled Monolayers. *RSC Adv.* **2016**, *6*, 76110−76112.

(26) Kovalchuk, A.; Abu-Husein, T.; Fracasso, D.; Egger, D. A.; Zojer, E.; Zharnikov, M.; Terfort, A.; Chiechi, R. C. Transition Voltages Respond to Synthetic Reorientation of Embedded Dipoles in Self-Assembled Monolayers. *Chem. Sci.* **2016**, *7*, 781−787.

(27) Taucher, T. C.; Hehn, I.; Hofmann, O. T.; Zharnikov, M.; Zojer, E. Understanding Chemical versus Electrostatic Shifts in X-ray Photoelectron Spectra of Organic Self-Assembled Monolayers. *J. Phys. Chem. C* **2016**, *120*, 3428−3437.

(28) Lü, J.; Delamarche, E.; Eng, L.; Bennewitz, R.; Meyer, E.; Güntherodt, H.-J. Kelvin Probe Force Microscopy on Surfaces: Investigation of the Surface Potential of Self-Assembled Monolayers on Gold. *Langmuir* **1999**, *15*, 8184−8188.

(29) Chidsey, C. E. D.; Loiacono, D. N. Chemical Functionality in Self-Assembled Monolayers: Structural and Electrochemical Properties. *Langmuir* **1990**, *6*, 682−691.

(30) Lemal, D. M. Perspective on Fluorocarbon Chemistry. *J. Org. Chem.* **2004**, *69*, 1−11.

(31) Zenasni, O.; Marquez, M. D.; Jamison, A. C.; Lee, H. J.; Czader, A.; Lee, T. R. Inverted Surface Dipoles in Fluorinated Self-Assembled Monolayers. *Chem. Mater.* **2015**, *27*, 7433−7446.

(32) Chiechi, R. C.; Weiss, E. A.; Dickey, M. D.; Whitesides, G. M. Eutectic Gallium−Indium (EGaIn): A Moldable Liquid Metal for Electrical Characterization of Self-Assembled Monolayers. *Angew. Chem., Int. Ed.* **2008**, *47*, 142−144.

(33) te Velde, G.; Bickelhaupt, F. M.; Baerends, E. J.; Guerra, C. F.; van Gisbergen, S. J. A.; Snijders, J. G.; Ziegler, T. Chemistry with ADF. *J. Comput. Chem.* **2001**, *22*, 931−967.

(34) ADF2016, SCM, Theoretical Chemistry; Vrjie Universiteit: Amsterdam, The Netherlands. https://www.scm.com, accessed Dec 1, 2017.

(35) Guerra, C. F.; Snijders, J. G.; te Velde, G.; Baerends, E. J. Towards an Order-N DFT Method. *Theor. Chem. Acc.* **1998**, *99*, 391−403.

(36) van Lenthe, E.; Baerends, E. J. Optimized Slater-type basis sets for the elements 1-118. *J. Comput. Chem.* **2003**, *24*, 1142−1156.

(37) Stephens, P. J.; Devlin, F. J.; Chabalowski, C. F.; Frisch, M. J. Ab Initio Calculation of Vibrational Absorption and Circular Dichroism Spectra Using Density Functional Force Fields. *J. Phys. Chem.* **1994**, *98*, 11623−11627.

(38) Grimme, S.; Antony, J.; Ehrlich, S.; Krieg, H. A Consistent and Accurate Ab Initio Parametrization of Density Functional Dispersion Correction (DFT-D) for the 94 Elements H-Pu. *J. Chem. Phys.* **2010**, *132*, 154104.

(39) Kahn, A. Fermi Level, Work Function and Vacuum Level. *Mater. Horiz.* **2016**, *3*, 7−10.

(40) Natan, A.; Kronik, L.; Haick, H.; Tung, R. T. Electrostatic Properties of Ideal and Non-Ideal Polar Organic Monolayers: Implications for Electronic Devices. *Adv. Mater.* **2007**, *19*, 4103−4117.

(41) Alloway, D. M.; Graham, A. L.; Yang, X.; Mudalige, A.; Colorado, R.; Wysocki, V. H.; Pemberton, J. E.; Lee, T. R.; Wysocki, R. J.; Armstrong, N. R. Tuning the Effective Work Function of Gold and Silver Using ω-Functionalized Alkanethiols: Varying Surface Composition through Dilution and Choice of Terminal Groups. *J. Phys. Chem. C* **2009**, *113*, 20328−20334.

(42) Alves, C. A.; Porter, M. D. Atomic Force Microscopic Characterization of a Fluorinated Alkanethiolate Monolayer at Gold and Correlations to Electrochemical and Infrared Reflection Spectroscopic Structural Descriptions. *Langmuir* **1993**, *9*, 3507−3512.

(43) Alloway, D. M.; Hofmann, M.; Smith, D. L.; Gruhn, N. E.; Graham, A. L.; Colorado, R., Jr.; Wysocki, V. H.; Lee, T. R.; Lee, P. A.; Armstrong, N. R. Interface Dipoles Arising from Self-Assembled Monolayers on Gold: UV-Photoemission Studies of Alkanethiols and Partially Fluorinated Alkanethiols. *J. Phys. Chem. B* **2003**, *107*, 11690−11699.

(44) Osella, S.; Cornil, D.; Cornil, J. Work Function Modification of the (111) Gold Surface Covered by Long Alkanethiol-Based Self-Assembled Monolayers. *Phys. Chem. Chem. Phys.* **2014**, *16*, 2866−2873.

(45) Houston, J. E.; Doelling, C. M.; Vanderlick, T. K.; Hu, Y.; Scoles, G.; Wenzl, I.; Lee, T. R. Comparative Study of the Adhesion, Friction, and Mechanical Properties of CF3- and CH3-Terminated Alkanethiol Monolayers. *Langmuir* **2005**, *21*, 3926−3932.

(46) Lovat, G.; Choi, B.; Paley, D. W.; Steigerwald, M. L.; Venkataraman, L.; Roy, X. Room-Temperature Current Blockade in Atomically Defined Single-Cluster Junctions. *Nat. Nanotechnol.* **2017**, *12*, 1050−1054.

(47) Niskala, J. R.; Rice, W. C.; Bruce, R. C.; Merkel, T. J.; Tsui, F.; You, W. Tunneling Characteristics of Au−Alkanedithiol−Au Junctions formed via Nanotransfer Printing (nTP). *J. Am. Chem. Soc.* **2012**, *134*, 12072−12082.

(48) Jeong, H.; Kim, D.; Xiang, D.; Lee, T. High-Yield Functional Molecular Electronic Devices. *ACS Nano* **2017**, *11*, 6511−6548.

(49) Xiang, D.; Wang, X.; Jia, C.; Lee, T.; Guo, X. Molecular-Scale Electronics: From Concept to Function. *Chem. Rev.* **2016**, *116*, 4318−4440.

(50) Pookpanratana, S.; Robertson, J. W. F.; Jaye, C.; Fischer, D. A.; Richter, C. A.; Hacker, C. A. Electrical and Physical Characterization of Bilayer Carboxylic Acid-Functionalized Molecular Layers. *Langmuir* **2013**, *29*, 2083−2091.

(51) Sangeeth, C. S. S.; Wan, A.; Nijhuis, C. A. Equivalent Circuits of a Self-Assembled Monolayer-Based Tunnel Junction Determined by Impedance Spectroscopy. *J. Am. Chem. Soc.* **2014**, *136*, 11134−11144.

(52) Vilan, A.; Aswal, D.; Cahen, D. Large-Area, Ensemble Molecular Electronics: Motivation and Challenges. *Chem. Rev.* **2017**, *117*, 4248−4286.

(53) Heimel, G.; Romaner, L.; Zojer, E.; Brédas, J.-L. Toward Control of the Metal−Organic Interfacial Electronic Structure in Molecular Electronics: A First-Principles Study on Self-Assembled Monolayers of π-Conjugated Molecules on Noble Metals. *Nano Lett.* **2007**, *7*, 932−940.

(54) Beebe, J. M.; Moore, H. J.; Lee, T. R.; Kushmerick, J. G. Vibronic Coupling in Semifluorinated Alkanethiol Junctions: Implications for Selection Rules in Inelastic Electron Tunneling Spectroscopy. *Nano Lett.* **2007**, *7*, 1364−1368.

(55) Qi, Y.; Yaffe, O.; Tirosh, E.; Vilan, A.; Cahen, D.; Kahn, A. Filled and Empty States of Alkanethiol Monolayer on Au (111): Fermi Level Asymmetry and Implications for Electron Transport. *Chem. Phys. Lett.* **2011**, *511*, 344−347.

(56) Qiu, L.; Zhang, Y.; Krijger, T. L.; Qiu, X.; van't Hof, P.; Hummelen, J. C.; Chiechi, R. C. Rectification of Current Responds to Incorporation of Fullerenes into Mixed-Monolayers of Alkanethiolates in Tunneling Junctions. *Chem. Sci.* **2017**, *8*, 2365−2372.

■ NOTE ADDED AFTER ASAP PUBLICATION

Grammatical and punctuation changes were made on February 27, 2018.